chemistry by either: (1) raising total alkalinity (alk_t) (where alkalinity = $[HCO_3^-] + 2[CO_3^{2-}] + [HBO_3^-]$) to constant levels of $2,842 \pm 80\ \mu eq\ kg^{-1}$ (equivalent = mole of negative or positive charge) ($n = 29$ groups) (ambient $alk_t = 2,241 \pm 19\ \mu eq\ kg^{-1}$; $n = 64$ groups) and letting ΣCO_2 ($\Sigma CO_2 = [CO_2] + [HCO_3^-] + [CO_3^{2-}]$) and pH vary (pH ranges between 7.38 and 8.83); or (2) keeping ΣCO_2 constant at $2,032 \pm 15\ \mu mol\ kg^{-1}$ ($n = 15$ groups) (ambient $\Sigma CO_2 = 2,010 \pm 18\ \mu mol\ kg^{-1}$; $n = 64$ groups) and letting pH and alkalinity vary (pH ranges from 7.87 to 8.97). For comparison with our experiments, pH and $[CO_3^{2-}]$ in Southern California Bight surface waters varied between 8.11–8.19 and 153–184 $\mu mol\ kg^{-1}$ during our field campaign.

Seawater ΣCO_2 and alk_t were modified by the addition of Na_2CO_3 and/or titration with HCl or NaOH to bring alk_t to desired levels. Seawater pH was determined by potentiometry whereas alk_t and ΣCO_2 were determined by titration and equilibrium calculations respectively. Coulometric determinations of several seawater samples confirm the accuracy of the calculated ΣCO_2 values (A. Sanyal, personal communication). Culture water samples collected at the start and end of each experiment showed that alkalinity and ΣCO_2 remained constant throughout each experiment.

Stable isotope analyses. Individual *O. universa* shells and *G. bulloides* chambers were roasted at 375 °C *in vacuo* and analysed with a Fisons Optima isotope ratio mass spectrometer using an Isocarb common acid bath autocarbonate system at 90 °C. Here $\delta^{18}O = [(^{18}O/^{16}O_{sample}/^{18}O/^{16}O_{std}) - 1]$ and $\delta^{13}C = [(^{13}C/^{12}C_{sample}/^{13}C/^{12}C_{std}) - 1]$. All $\delta^{13}C_{\Sigma CO_2}$ and $CaCO_3$ isotope values are relative to the V-PDB standard. Water samples collected at the start and end of each experiment show that $\delta^{18}O_{water}$ was constant at -0.23 ± 0.05‰ (relative to the V-SMOW standard) ($n = 100$) whereas initial and final water $\delta^{13}C_{\Sigma CO_2}$ differed on average by 0.16 ± 0.10‰ ($n = 30$). All foraminiferal $\delta^{13}C$ data have been corrected to a constant $\delta^{13}C_{\Sigma CO_2} = 2.00$‰ (ambient $\delta^{13}C_{\Sigma CO_2}$ was 1.90 ± 0.08‰, $n = 18$) to account for $\delta^{13}C_{\Sigma CO_2}$ differences between treatments due to the addition of Na_2CO_3.

Received 6 January; accepted 7 October 1997.

1. Epstein, S., Buchsbaum, R., Lowenstam, H. A. & Urey, H. C. Revised carbonate-water isotopic temperature scale. *Geol. Soc. Am. Bull.* **64,** 1315–1325 (1953).
2. Spero, H. J., Lerche, I. & Williams, D. F. Opening the carbon isotope "vital effect" black box, 2: Quantitative model for interpreting foraminiferal carbon isotope data. *Paleoceanography* **6,** 639–655 (1991).
3. Shackleton, N. J. & Opdyke, N. D. Oxygen isotope and palaeomagnetic stratigraphy of equatorial Pacific core V28-238: Oxygen isotope temperatures and ice volumes on a 10^5 year and 10^6 year scale. *Quat. Res.* **3,** 39–55 (1973).
4. Broecker, W. S. Oxygen isotope constraints on surface ocean temperatures. *Quat. Res.* **26,** 121–134 (1986).
5. Labeyrie, L. D., Duplessy, J.-C. & Blanc, P. L. Variations in mode of formation and temperature of oceanic deep waters over the past 125,000 years. *Nature* **327,** 477–482 (1987).
6. Duplessy, J. C. *et al.* Deepwater source variations during the last climatic cycle and their impact on the global deepwater circulation. *Paleoceanography* **3,** 343–360 (1988).
7. Shackleton, N. J. Carbon-13 in Uvigerina: tropical rainsforest history and the equatorial Pacific carbonate dissolution cycles. in *The Fate of Fossil Fuel CO_2 in the Oceans* (eds Andersen, N. R. & Malahoff, A.) 401–427 (Plenum, New York, 1977).
8. Sanyal, A., Hemming, N. G., Hanson, G. N. & Broecker, W. S. Evidence for a higher pH in the glacial ocean from boron isotopes in foraminifera. *Nature* **373,** 234–236 (1995).
9. Kaufman, A. J., Jacobsen, S. B. & Knoll, A. H. The Vendian record of Sr and C isotopic variations in seawater: Implications for tectonics and paleoclimate. *Earth Planet. Sci. Lett.* **120,** 409–430 (1993).
10. Fairbanks, R. G., Sverdlove, M., Free, R., Wiebe, P. H. & Be, A. W. H. Vertical distribution and isotopic fractionation of living planktonic foraminifera from the Panama Basin. *Nature* **298,** 841–844 (1982).
11. Spero, H. J. & Lea, D. W. Experimental determination of stable isotope variability in *Globigerina bulloides*: Implications for paleoceanographic reconstruction. *Mar. Micropaleontol.* **28,** 231–246 (1996).
12. McConnaughey, T. ^{13}C and ^{18}O isotopic disequilibrium in biological carbonates: II. In vitro simulation of kinetic isotope effects. *Geochim. Cosmochim. Acta* **53,** 163–171 (1989).
13. Spero, H. J. & Parker, S. L. Photosynthesis in the symbiotic planktonic foraminifer *Orbulina universa*, and its potential contribution to oceanic primary productivity. *J. Foram. Res.* **15,** 273–281 (1985).
14. Spero, H. J. Do planktic foraminifera accurately record shifts in the carbon isotopic composition of sea water ΣCO_2? *Mar. Micropaleontol.* **19,** 275–285 (1992).
15. McConnaughey, T. ^{13}C and ^{18}O isotopic disequilibrium in biological carbonates: I. Patterns. *Geochim. Cosmochim. Acta* **53,** 151–162 (1989).
16. Smith, J. E., Risk, M. J., Schwarcz, H. P. & McConnaughey, T. A. Rapid climate change in the North Atlantic during the Younger Dryas recorded by deep-sea corals. *Nature* **386,** 818–820 (1997).
17. Spero, H. J. & Lea, D. W. Intraspecific stable isotope variability in the planktic foraminifera *Globigerinoides sacculifer*: Results from laboratory experiments. *Mar. Micropaleontol.* **22,** 221–234 (1993).
18. McCrea, J. M. On the isotopic chemistry of carbonates and a paleotemperature scale. *J. Chem. Phys.* **18,** 849–857 (1950).
19. Zhang, J., Quay, P. D. & Wilbur, D. O. Carbon isotope fractionation during gas–water exchange and dissolution of CO_2. *Geochim. Cosmochim. Acta* **59,** 107–114 (1995).
20. Usdowski, E. & Hoefs, J. Oxygen isotope exchange between carbonic acid, bicarbonate, carbonate, and water: A re-examination of the data of McCrea (1950) and an expression for the overall partitioning of oxygen isotopes between the carbonate species and water. *Geochim. Cosmochim. Acta* **57,** 3815–3818 (1993).
21. McConnaughey, T. A., Burdett, J., Whelan, J. F. & Paull, C. K. Carbon isotopes in biological carbonates: Respiration and photosynthesis. *Geochim. Cosmochim. Acta* **61,** 611–622 (1997).
22. ter Kuile, B., Erez, J. & Padan, E. Mechanisms for the uptake of inorganic carbon by two species of symbiont-bearing foraminifera. *Mar. Biol.* **103,** 241–251 (1989).
23. Barnola, J. M., Raynaud, D., Korotkevich, Y. S. & Lorius, C. Vostock ice core provides 160,000-year record of atmospheric CO_2. *Nature* **329,** 408–413 (1987).
24. Broecker, W. S. & Peng, T.-H. What caused the glacial to interglacial CO_2 change? in *The Global Carbon Cycle* (ed. Heimann, M.) 95–115 (Springer, Berlin, 1993).
25. Lea, D. W., Spero, H. J., Bijma, J. & Archer, D. Implications of a carbonate ion effect on shell carbon and oxygen isotopes for glacial ocean conditions. *EOS* **77** (46) Fall Meeting Suppl. F334 (1996).
26. Shackleton, N. J., Hall, M. A., Line, J. & Shuxi, C. Carbon isotope data in core V19-30 confirm reduced carbon dioxide concentration in the ice age atmosphere. *Nature* **306,** 319–322 (1983).
27. Shackleton, N. J., Le, J., Mix, A. & Hall, M. A. Carbon isotope records from Pacific surface waters and atmospheric carbon dioxide. *Quat. Sci. Rev.* **11,** 387–400 (1992).
28. Crowley, T. J. Ice age terrestrial carbon changes revisited. *Global Biogeochem. Cycles* **9,** 377–389 (1995).
29. Guilderson, T. P., Fairbanks, R. G. & Rubenstone, J. L. Tropical temperature variations since 20,000 years ago: Modulating interhemispheric climate change. *Science* **263,** 663–665 (1994).
30. Thompson, L. G. *et al.* Late glacial stage and Holocene tropical ice core records from Huascaran, Peru. *Science* **269,** 46–50 (1995).
31. Berner, R. A. Geocarb II: A revised model of atmospheric CO_2 over Phanerozoic time. *Am. J. Sci.* **294,** 56–91 (1994).
32. Grotzinger, J. P. & Kasting, J. F. New constraints on Precambrian ocean composition. *J. Geol.* **101,** 235–243 (1993).
33. Wadleigh, M. A. & Veizer, J. $^{18}O/^{16}O$ and $^{13}C/^{12}C$ in Lower Paleozoic articulate brachiopods: Implications for the isotopic composition of seawater. *Geochim. Cosmochim. Acta* **56,** 431–443 (1992).

Acknowledgements. We thank the staff of the Wrigley Institute of Environmental Science and E. Kincaid, C. Hamilton, J. Dailey, E. Komsky, T. Mashiotta, M. Uhle, A. Sanyal, D. Chan, E. Mochon and M. Cramer for their help in the field. Thanks also to A. Russell and D. Sumner for comments on the manuscript. This research was supported by the US National Science Foundation (H.J.S. and D.W.L.) and by SFB 261 and the Program for the Advancement of Special Research Projects at the Alfred Wegener Institute, Germany (J.B.).

Correspondence should be addressed to H.J.S. (e-mail: spero@geology.ucdavis.edu).

Localization of the gravity field and the signature of glacial rebound

Mark Simons* & Bradford H. Hager

Department of Earth Atmospheric and Planetary Sciences, Massachusetts Institute of Technology, Cambridge, Massachusetts 02139, USA

The negative free-air gravity anomaly centred on Hudson Bay, Canada, shows a remarkable correlation with the location of the Laurentide ice sheet, suggesting that this gravity anomaly is the result of incomplete post-glacial rebound[1–3]. This region, however, is also underlain by higher-than-average mantle seismic velocities, suggesting that the gravity low might result instead from dynamic topography associated with convective downwellings[4–7]. Here we analyse the global gravity field as a simultaneous function of geographic location and spectral content. We find that the Hudson Bay gravity low is unique, with anomalously high amplitude in the spectral band where the power from the Laurentide ice load is greatest[2] and the relaxation times predicted for viable models of viscous relaxation are longest[8]. We estimate that about half of the Hudson Bay gravity anomaly is the result of incomplete post-glacial rebound, and derive a mantle viscosity model that explains both this gravity signature and the characteristic uplift rates for the central Laurentide and Fennoscandian regions[6]. This model has a jump in viscosity at 670 km depth, comparable to that in dynamic models of the geoid highs over subducted slabs[4,9], but lacks a low-viscosity asthenosphere, consistent with a higher viscosity in the upper mantle beneath shields than in oceanic regions.

Delayed rebound is not the dominant process generating variations in the global gravity field (Fig. 1a); many anomalies of comparable or greater amplitude than those in deglaciated areas

* Present address: Seismological Laboratory, California Institute of Technology, Pasadena, California 91125, USA.

Nature © Macmillan Publishers Ltd 1997

exist elsewhere. Indeed, there is a poor global correlation between the observed gravity field and that predicted by models of glacial isostasy[10,11]. Previous attempts to relate the observed gravity field to the glacial rebound process have focused either on the local amplitude of the gravity field[7,11] or on global correlations as a function of spherical harmonic degree[10,11]. Our approach relies on a spatio-spectral localization method for spherical harmonic representations of global data sets[12,13]. This method is similar to wavelet techniques in the cartesian domain and is well suited to global geophysical data. The method can be expressed as spatial windowing followed by spectral decomposition. We use a smooth axisymmetric window with a characteristic spatial width equal to twice the wavelength being considered. The window is translated over the globe providing sets of localized coefficients at all positions and wavelengths. Further details on this procedure, including the limitations imposed by using data with finite resolution, can be found elsewhere[12,13].

Maps of the spatially and spectrally localized r.m.s. amplitude of the gravity field, $S_l(\Omega)$, are shown in Fig. 1b. At $l = 4$ there is a broad maximum over central Asia, Indonesia, Australia and Antarctica, and two minima over Africa and the central Pacific. Regions of subduction are frequently associated with S_l highs. At $l \leqslant 9$ this high is associated with mantle convection processes[12,14] and at $l \geqslant 25$ with deep sea trenches. S_9 has a maximum over Hudson Bay. For $l \geqslant 9$, there are S_l maxima over the Andes, the Tibetan plateau and regions north of the plateau.

Spectrograms of the gravity field along two great-circle paths are shown in Fig. 1c–e. Hudson Bay is unique in that it is characterized by a gravity anomaly that is localized both in space and in length scale, with a peak ΔS_l value at $l \approx 9$, corresponding to length scales of ~4,200 km. In contrast with Hudson Bay, regions containing steep gradients in the gravity field, such as the Himalayas, are characterized by spatially localized spectral ridges. For the Himalayas, the spectral ridge extends down to $l \approx 10$, or to wavelengths as great as 4,000 km. The Sri Lankan low is part of a larger-length-scale low, extending from south of Australia to central Asia, that is

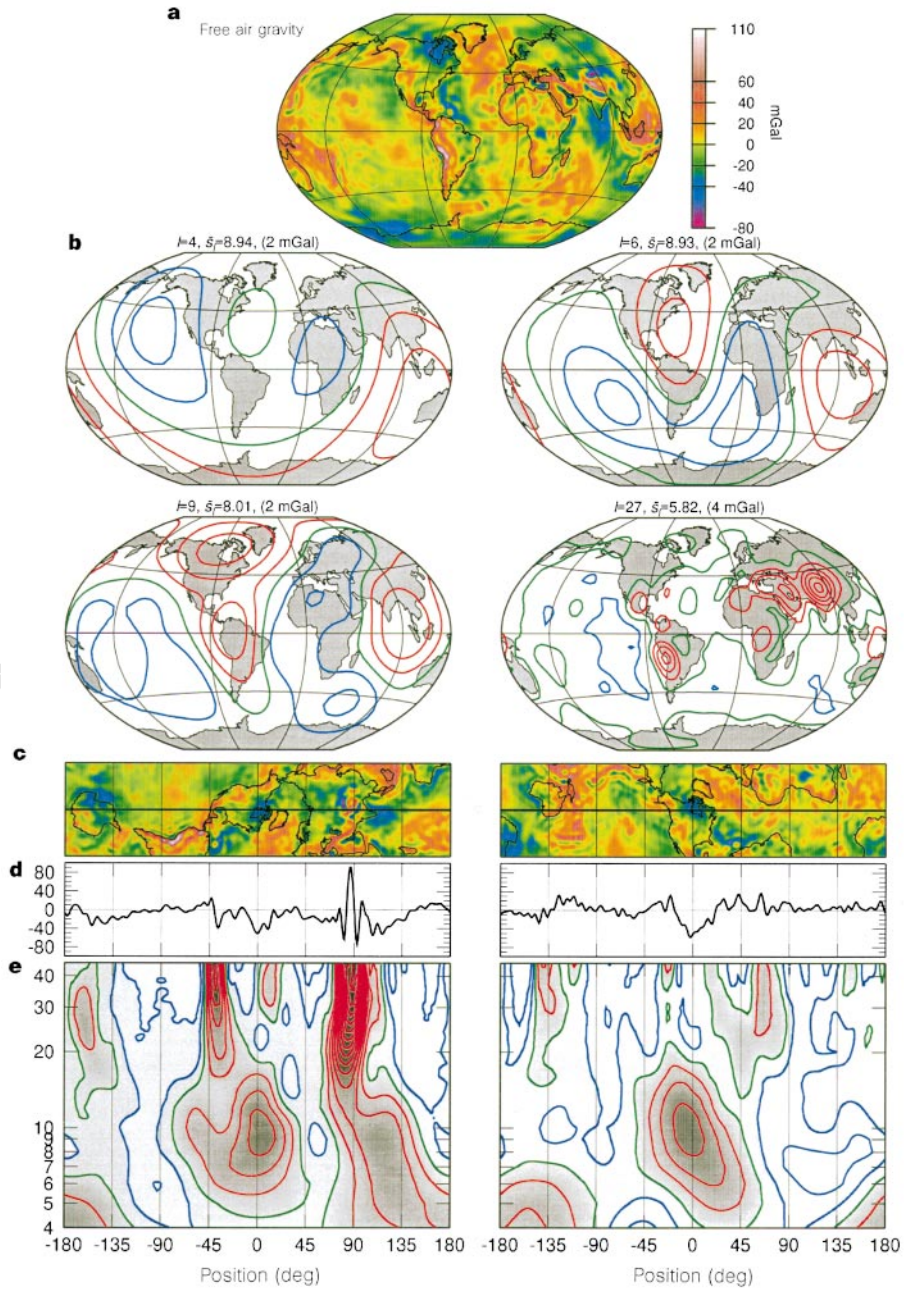

Figure 1 Spatio-spectral renditions of the gravity field. **a**, Spatial rendition of the free air gravity field from spherical harmonic model JGM-2G (refs 24, 25). For this figure, the coefficients for the gravity field have been smoothly tapered from $l = 50$–70. The analysis presented here has been conducted with both a free-air gravity and a geoid representation. Although we focus on the former representation, the conclusions do not depend on this choice. A Winkel Tripel projection centred at 45° W is used for all global maps shown here. **b**, Maps of $\Delta S_l(\Omega)$ for selected l, where $\Delta S_l(\Omega) = S_l(\Omega) - \bar{S}_l$ and $\bar{S}_l$ is the global average of $S_l(\Omega)$. $\bar{S}_l$ and the contour interval are indicated at the top of each diagram. $\Delta S_l > 0$, $\Delta S_l = 0$ and $\Delta S_l > 0$ are indicated by red, green and blue contours, respectively. Note that ΔS_l is a measure of the variation, but not the sign, of the original signal. **c**, Location maps for the two great-circle S_l spectrograms (chosen to be nearly orthogonal at Hudson Bay). Oblique Mercator projection for which the Equator is the great circle path indicated by the horizontal line. **d**, Gravity profiles along the great-circle paths. The localization uses the full two-dimensional field. **e**, ΔS_l as a function of l and position along the great circle. Same line convention as in **b**, with a 2 mGal contour interval[26].

Nature © Macmillan Publishers Ltd 1997

interrupted by a short-length-scale positive anomaly over the Himalayas and Tibet. The short-length-scale anomaly is presumably related to crustal thickness variations, whereas the longer-length-scale negative anomaly is due to deeper convective processes. Unlike the Hudson Bay low, the Sri Lankan low has a spectral maximum extending down to the smallest l considered. Another spectral ridge, extending down to $l \approx 13$, is found traversing central America, again presumably related to the large variation in crustal thickness. Over the same region, S_l has a minimum at $l \approx 10$ and then increases again at lower l, due to the effects of the subducting slab at the Middle American subduction zone[14]. In contrast with the large S_l associated with deglaciated regions and subduction zones, we find no obvious signals at low degrees associated with hotspots. The South Pacific area is notable because it appears as a minimum in the estimates of S_l of the gravity field at all wavelengths.

Unlike for the gravity field, for seismic tomography models (for example, ref. 15) at depths between 100 and 300 km, estimates of S_l at $l = 6$–11 do not have a unique maximum associated with Hudson Bay (see Supplementary Information). Therefore, although there is probably a convective component to the total gravity anomaly in Hudson Bay, a significant portion of this anomaly is apparently related to glacial rebound. Unfortunately, it is difficult to separate the individual contributions to the gravity field from convection and incomplete glacial rebound. Furthermore, models of both of these processes are highly dependent on the rheological structure assumed[4,9,14,16–19], and the success of these models has been limited by their reliance on global variance reduction or spatial amplitude to measure their performance. By necessity, this reliance implies that one is also modelling gravity anomalies that are unrelated to the process being considered. Here, we take an approach that is based on the local correlation between the observed gravity field, $N(\Omega)$, and the spatial distribution of a tectonic process, $T(\Omega)$, in this case the amplitude of deglaciation at a particular position. We calculate the local l-dependent transfer function, $F_l(\Omega)$, between $T(\Omega)$ and $N(\Omega)$ over the entire planet. A single global transfer function, $\tilde{F}_l$, is derived by spatially averaging $F_l(\Omega)$ weighted by the local variance, $S_l^2(\Omega)$, of $T(\Omega)$, to emphasize regions that have experienced deglaciation. A predicted gravity field can then be created by convolving $\tilde{F}_l$ with the harmonic coefficients of $T(\Omega)$. In practice, we choose $T(\Omega)$ to be the gravity field due to instantaneous deglaciation if there had been no viscous relaxation. We refer to this choice of $T(\Omega)$ as $N^{\mathrm{inst}}(\Omega)$, constructed by assuming isostatic equilibrium before deglaciation and uniform redistribution of the melted ice load over the ocean basins.

$\tilde{F}_l$ describes the relation between the observed gravity field and N^{inst}. Because our initial distribution function, N^{inst}, is that corresponding to no relaxation, we should find that $\tilde{F}_l < 1$ for all l. We also calculate the analogous quantity, $\tilde{F}_l^{\mathrm{M}}$, describing the relation between N^{inst} and predictions of the present-day glacial rebound gravity field from a suite of viscosity models (Fig. 2a). Comparison of data and models is done by using $\tilde{F}_l$ because the models should be judged only after submitting them to the same filtering as the data.

To determine the model predictions of the present-day glacial rebound gravity field, we calculate the relaxation spectrum, τ_l^{M}, for each viscosity model assuming that the mantle can be described as a spherically symmetric newtonian fluid underlying a thin elastic lithosphere of thickness h (ref. 2). We consider three previously published viscosity models (LJN (ref. 20), HC (ref. 4) and FM (ref.

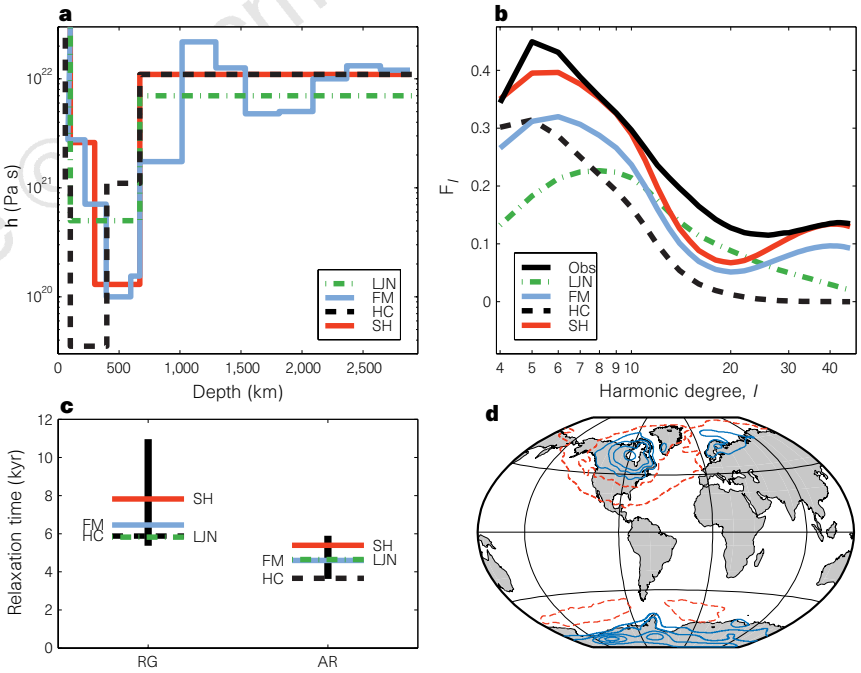

Figure 2 Viscosity model predictions versus observation. **a**, Viscosity, η, plotted against depth for models LJN, HC, FM and SH. All models use a 100-km-thick elastic surface layer, h, except model HC, which has $h = 60$ km. **b**, Observed and model predictions of $\tilde{F}_l$. The estimates of ice thickness are taken from the ICE-3G deglaciation history[27]. In estimating $\tilde{F}_l$ we have made a simple correction to the observed gravity field, N^{obs}, for crustal thickness variations, ocean–continent differences and oceanic plate cooling[28]. We also reference both N^{inst} and N^{obs} to the best-fitting ellipsoid. We make this choice because localization (using a window with characteristic length scale twice of that being considered) is not possible at $l = 2$. In particular, because N^{inst} is focused at the poles, it will have a significant correlation with the c_{20} term of N^{obs}, whether actually caused by glacial rebound or by other processes, including convection or the delayed readjustment of the hydrostatic figure to changes in rotation rate[10]. Furthermore, because localization reduces spectral resolution, any difficulties at $l = 2$ can bleed into the neighbouring degrees. Therefore, we only consider here estimates of $\tilde{F}_l$ for $l \geq 4$. **c**, Point relaxation times from RSL data at Richmond Gulf (RG) and Angerman River (AR). The vertical lines indicate the observed values with their errors[21], and the horizontal lines indicate predictions from the indicated viscosity models. Model predictions are based on the best-fitting exponential to the elevations at AR and RG over the last 6 kyr. **d**, Predicted gravity field due to incomplete rebound with viscosity model SH; 6 mGal contour interval with solid and broken lines for contours $\leq$3 mGal and $\geq$3 mGal, respectively.

Nature © Macmillan Publishers Ltd 1997

Nature © Macmillan Publishers Ltd 1997

6)) as well as a new model (SH) that we developed specifically to fit the estimates of $\tilde{F}_l$. The viscosity models are shown in Fig. 2a. Each τ_l^M spectrum is convolved with the deglaciation history to generate a predicted gravity model, N^M. The globally averaged local transfer function, $\tilde{F}_l^M$, between N^{inst} and N^M can then be compared with $\tilde{F}_l$ (Fig. 2b).

Model LJN (ref. 20) is from a study of relative sea level (RSL) data in northwest Europe and uses no gravity data. This three-layer model considerably underestimates $\tilde{F}_l$ at low l. The discrepancy indicates that either the longest wavelengths are poorly constrained by the RSL data or that the longest wavelengths of $\tilde{F}_l$ are dominated by Hudson Bay and are not representative of the longest wavelengths in Fennoscandia.

Viscosity model HC has four viscous layers and is derived from a mantle flow calculation with a model of subducting lithosphere and lower-mantle seismic tomography as the buoyancy distribution[4]. Such flow models, used to infer viscosity distributions based on fits to the geoid, are sensitive only to relative viscosity variations and not to the absolute viscosity. To facilitate later comparisons we assign a lower-mantle viscosity to model HC of 1.1×10^{22} Pa s, which is taken directly from our new model SH. The salient feature of HC is the low (relative to the lower mantle) viscosities in the asthenosphere and transition zone. This viscosity variation was invoked to match the observed geoid anomalies over subduction zones[4]. This model consistently underestimates $\tilde{F}_l$ and lacks the increase in $\tilde{F}_l$ at high l.

Model FM (ref. 6) is from a joint inversion of RSL data at Angerman River (AR), Sweden, and Richmond Gulf (RG), Canada, together with a dynamic flow calculation done in a manner similar to that of HC, but by using a model of mantle heterogeneity inferred exclusively from seismic tomography. The dynamic flow component of the inversion attempts to fit only the $l = 2$–8 components of the gravity field. This model has 13 viscosity layers. Of the models discussed so far, FM matches the shape of the observed $\tilde{F}_l$ estimates the best, with maxima occurring at the same degrees. Despite the use of RSL data as calibration for the absolute viscosity, model FM also consistently underestimates $\tilde{F}_l$. However, because model FM uses a global seismic tomography model of both the upper and lower mantle as input, it should be considered as a global model applying both to oceanic and continental regions.

Using forward modelling, we have found a three-layer viscosity model (SH) that adequately fits the $\tilde{F}_l$ spectrum. The salient features of SH are the relatively high viscosity of the lower mantle (1.1×10^{22} Pa s) driven by the need to match the high values of $\tilde{F}_l$ at low degrees, the low viscosity in the transition zone, and the 300 km thickness of the high-viscosity layer (2.6×10^{21} Pa s) in the upper mantle. A reduction in the thickness or magnitude of this upper-mantle high-viscosity layer degrades the fit to $\tilde{F}_l$. The thick high-viscosity layer can also be found in model FM, and contrasts with models such as HC, which are based on flow models with the source of buoyancy in the upper mantle restricted to subduction zone environments. The logarithmic average of the upper-mantle viscosities in SH and FM is very near the upper-mantle value in model LJN, which has a single layer for the entire sub-lithospheric upper mantle. All the viscosity models fail to match $\tilde{F}_l$ near $l = 18$. Although the use of additional layers in SH could reduce this misfit, additional parameters are unwarranted given the simplicity of our modelling approach.

As an independent check on our viscosity model, we also consider the sea-level data used in constructing the LJN and FM models. We use relaxation times for two sites chosen by Mitrovica[21] and Forte and Mitrovica[6] for AR and RG (Fig. 2c). These two sites were chosen because of their proximity to the centres of regions of deglaciation, thereby limiting their sensitivity to details in the model of deglaciation as well as limiting possible complications stemming from lateral variations in viscosity at the edges of the continents. The spatial relaxation times for AR, τ^{AR}, and RG, τ^{RG}, are ~4.7 and 7.6 kyr, respectively[6,21], although recent studies of other sea-level records in both of these areas indicate a spread of relaxation times[22]. These times are estimates at single points and represent the sum over all the wavelengths present at each location, thereby complicating any direct comparison with $\tilde{F}_l$. We find that all the viscosity models fit within the range of acceptable values and that the differences between model prediction for τ^{AR} and τ^{RG} are entirely consistent with the differences in their estimates of $\tilde{F}_l$. That model SH fits both the gravity and uplift data at Richmond Gulf but is near the upper bound of relaxation times for Angerman River might be indicative of variations in viscosity between the two sites.

When judging the success of a given viscosity model, the peak spatial gravity anomaly is a dangerous quantity to use because two different models can predict the same peak anomaly but with very different spectral contents (this is analogous to the non-uniqueness of the point RSL measurements). However, given a viscosity model, we can ask what portion of the total spatial gravity field is predicted to be due to incomplete rebound. Over Hudson Bay, model SH predicts a peak gravity anomaly of −24 mGal (Fig. 2d) and a peak geoid anomaly of −31 m. These values are just under half the total spatial gravity anomaly and over one-third of the total geoid anomaly in Hudson Bay. Over Fennoscandia, model SH predicts a peak gravity anomaly of about −10 mGal (Fig. 2d) and a peak geoid anomaly of about −6 m. Over Antarctica, model SH predicts a gravity anomaly of about −30 mGal and a geoid anomaly of about −26 m. These large anomalies probably reflect the relatively late deglaciation that is associated with the Antarctic ice sheet[23]. The observed, predicted and residual gravity and geoid are shown in the Supplementary Information.

Viewed globally, the observed geoid and gravity fields have red spectra[1]. This long-wavelength bias complicates any spatial analysis. Viewed locally, spectra vary greatly as a function of position—a reflection of the different geophysical processes that are active within a given region. To address this spatio-spectral complexity, we use a new localization method that renders more information than approaches that are either purely spatial or purely spectral. Because we are free to choose the extent of localization in either domain, our choice is non-unique. The spatio-spectral description presented here isolates the contribution to the gravity field from mantle convection, lithospheric-scale processes and incomplete glacial rebound. The rebound signature is greater than recent estimates and can be used to constrain models of mantle viscosity. We propose one such model that, although designed to explain the rebound portion of the gravity field, also matches observed RSL relaxation times. This model is characterized by a higher upper-mantle viscosity than viscosity models that explain the geoid highs associated with subducted slabs, consistent with a higher viscosity under shields than beneath oceans and continental margins. □

Received 27 January; accepted 23 September 1997.

1. Kaula, W. M. in *The Nature of the Solid Earth* (ed. Robertson, E. C.) 385–405 (McGraw-Hill, New York, 1972).
2. Walcott, R. I. Structure of the earth from glacio-isostatic rebound. *Annu. Rev. Earth. Planet. Sci.* **1,** 15–37 (1973).
3. Cathles, L. M. *The Viscosity of the Earth's Mantle* (Princeton Univ. Press, 1975).
4. Hager, B. H. & Clayton, R. W. in *Mantle Convection* (ed. Peltier, W. R.) 657–763 (Gordon and Breach, New York, 1989).
5. Peltier, W. R., Forte, A. M., Mitrovica, J. X. & Dziewonski, A. M. Earth's gravitational field: seismic tomography resolves the enigma of the Laurentian anomaly. *Geophys. Res. Lett.* **19,** 1555–1558 (1992).
6. Forte, A. M. & Mitrovica, J. X. New inferences of mantle viscosity from joint inversion of long-wavelength mantle conveciton and post-glacial rebound data. *Geophys. Res. Lett.* **23,** 1147–1150 (1996).
7. Pari, G. & Peltier, W. R. The free-air gravity constraint on subcontinental mantle dynamics. *J. Geophys. Res.* **101,** 28105–28132 (1996).
8. Hager, B. H. in *Glacial Isostasy, Sea-level and Mantle Rheology* (eds R. Sabadini, K. L. & Boschi, E.) 493–513 (*NATO ASI Ser. C.* vol. 334, Kluwer, Dordrecht, 1991).
9. Ricard, Y. & Vigny, C. Mantle dynamics with induced plate tectonics. *J. Geophys. Res.* **94,** 17543–17559 (1989).
10. O'Connell, R. J. Pleistocene glaciation and the viscosity of the mantle. *Geophys. J. R. Astron. Soc.* **23,** 299–327 (1971).
11. Mitrovica, J. X. & Peltier, W. R. Pleistocene deglaciation and the global gravity field. *J. Geophys. Res.* **94,** 13651–13671 (1989).
12. Simons, M. thesis, MIT, Cambridge, Massachusetts (1996).

Nature © Macmillan Publishers Ltd 1997

13. Simons, M., Solomon, S. C. & Hager, B. H. Localization of gravity and topography: constraints on the tectonics and mantle dynamics of Venus. *Geophys. J. Int.* **131,** 24–44 (1997).
14. Hager, B. H. Subducted slabs and the geoid: constraints on mantle rheology and flow. *J. Geophys. Res.* **89,** 6003–6015 (1984).
15. Masters, G., Johnson, S., Laske, G. & Bolton, H. A shear-velocity model of the mantle. *Phil. Trans. R. Soc. Lond. A* **354,** 1385–1411 (1996).
16. Van Bemmelen, R. W. & Berlage, H. P. Versuch einer mathematischen behandlung geotektonischer bewegung unter besonderer berucksichtegung der undationstheorie. *Beitr. Geophys.* **43,** 19–55 (1935).
17. Haskell, N. A. The viscosity of the asthenosphere. *Am. J. Sci.* **33,** 22–28 (1937).
18. Forte, A. M. & Peltier, W. R. Viscous flow models of global geophysical observables. 1. Forward problems. *J. Geophys. Res.* **96,** 20131–20159 (1991).
19. Forte, A. M., Woodward, R. L. & Dziewonski, A. M. Joint inversions of seismic and geodynamic data for models of three-dimensional mantle heterogeneity. *J. Geophys. Res.* **99,** 21857–21877 (1994).
20. Lambeck, K., Johnston, P. & Nakada, M. Glacial rebound and sea-level change in northwestern europe. *Geophys. J. Int.* **103,** 451–468 (1990).
21. Mitrovica, J. X. Haskell [1935] revisited. *J. Geophys. Res.* **101,** 555–569 (1996).
22. Mitrovica, J. X. & Forte, A. M. Radial profile of mantle viscosity—results from the joint inversion of convection and postglacial rebound observables. *J. Geophys. Res.* **102,** 2751–2769 (1997).
23. Nakada, M. & Lambeck, K. Glacial rebound and relative sea-level variations: a new appraisal. *Geophys. J. R. Astron. Soc.* **90,** 171–224 (1987).
24. Nerem, R. S. *et al.* Gravity model development for TOPEX/Poseidon: joint gravity models 1 and 2. *J. Geophys. Res.* **99,** 24421–24447 (1994).
25. Nerem, R. S., Jekeli, C. & Kaula, W. M. Gravity field determination and characteristics: retrospective and prospective. *J. Geophys. Res.* **100,** 15053–15074 (1995).
26. Wessel, P. & Smith, W. H. F. New version of the Generic Mapping Tools released. *Eos* **76,** 329 (1991).
27. Tushingham, A. M. & Peltier, W. R. Ice-3g: a new global model of late Pleistocene deglaciation based upon geophysical predictions of post-glacial relative sea-level change. *J. Geophys. Res.* **96,** 4497–4523 (1991).
28. Hager, B. H. Global isostatic geoid anomalies for plate and boundary layer models of the lithosphere. *Earth Planet. Sci. Lett.* **63,** 97–109 (1983).

Supplementary Information is available on *Nature*'s World-Wide Web site (http://www.nature.com) or as paper copy from Mary Sheehan at the London editorial office of *Nature*.

Acknowledgements. We thank M. Fang, M. Gurnis and S. Zhong for constructive discussions, as well as J. X. Mitrovica for a thorough review. This work was supported by NASA.

Correspondence should be addressed to M.S. (e-mail: simons@gps.caltech.edu).

Cosmopolitanism among Gondwanan Late Cretaceous mammals

David W. Krause*, G. V. R. Prasad†, Wighart von Koenigswald‡, Ashok Sahni§ & Frederick E. Grine‖

* *Department of Anatomical Sciences, and* ‖ *Departments of Anthropology and Anatomical Sciences, State University of New York at Stony Brook, Stony Brook, New York 11794, USA*
† *Department of Geology, University of Jammu, Jammu 180 004, India*
‡ *Institute of Palaeontology, University of Bonn, Nussallee 8, D-53115, Bonn, Germany*
§ *Centre of Advanced Study in Geology, Panjab University, Chandigarh 160 014, India*

Consistent with geophysical evidence for the breaking up of Pangaea, it has been hypothesized that Cretaceous vertebrates on progressively isolated landmasses exhibit generally increasing levels of provincialism[1–3], with distinctly heightened endemism occurring at the beginning of the Late Cretaceous[4]. The Cretaceous fossil record from the southern supercontinent of Gondwana has been much too poor to test this hypothesis with regards to mammals (Fig. 1). Early Cretaceous mammals are known only from isolated sites in Argentina[5], Australia[6,7], Cameroon[8,9] and Morocco[10]. Apart from several occurrences in South America[11], knowledge of Late Cretaceous Gondwanan mammals is limited to a single site in India that previously yielded a few specimens of placental mammals[12,13], and a site in Madagascar that previously yielded only one indeterminate tooth fragment[14]. Here we report the occurrence of a highly specialized and distinctive group of extinct mammals, the Sudamericidae (Gondwanatheria), in the Late Cretaceous of Madagascar and India. These new records comprise the first evidence of gondwanatheres outside South America and the first indication of cosmopolitanism among Late Cretaceous Gondwanan mammals. Antarctica may have served as an important Cretaceous biogeographic link between South America and Indo-Madagascar.

The Gondwanatheria is a group of multituberculate[15,16]or multituberculate-like[17] mammals previously known only from the Late Cretaceous and Palaeocene of Argentina. Apart from two tentatively referred, fragmentary dentaries (one edentulous and the other bearing a single tooth), Gondwanatheria is based on isolated teeth. The gondwanathere teeth described here are the first identifiable, pre-Late Pleistocene specimens of non-marine mammals known from Madagascar and the first remains of non-placental mammals from the Cretaceous of the Indian subcontinent. The specimens from Madagascar were recovered during joint expeditions by the State University of New York, Stony Brook, and the Université d'Antananarivo in 1995 and 1996 to the continental Upper Cretaceous Maevarano Formation, which, in addition to mammals, has recently yielded a diversity of vertebrate taxa[18]. The gondwanathere specimen from India was discovered in 1989 in sediments of the Upper Cretaceous Deccan Intertrappean sequence[12,13], but was not identified as that of a gondwanathere until the specimens from Madagascar were examined. None of the lower taxa of mammals from the Late Cretaceous were previously known to be spread across South America, India and Madagascar.

Mammalia Linnaeus 1758
?Allotheria Marsh 1880
Gondwanatheria Mones 1987
Sudamericidae Scillato-Yané and Pascual 1984
Lavanify miolaka gen. et sp. nov.

Etymology. Lavanify (la-va-NEE-fee; Malagasy), long tooth; miolaka (MYOU-la-ka; Malagasy), curved; in reference to the shape of the cheek-teeth.

Holotype. Université d'Antananarivo (UA) 8653, well-preserved cheek-tooth (Fig. 2a, d).

Referred specimen. Field Museum of Natural History (FMNH) PM 59520, fragmentary cheek-tooth (Fig. 2b).

Localities and horizon. Holotype from locality MAD96-01 and referred specimen from locality MAD93-35, uppermost white sandstone unit of Upper Cretaceous (?Campanian) Maevarano Formation, Mahajanga Basin, near village of Berivotra, northwestern Madagascar.

Diagnosis. The teeth of *Lavanify* differ from those of the only previously known sudamericid genera *Gondwanatherium* and *Sudamerica* in possessing prominent and continuous inter-row sheets of interprismatic matrix in dental enamel and at least one cheek-tooth position that has a single, V-shaped dentine island and lacks enamel on one side of the crown. *Lavanify* further differs from *Gondwanatherium* in having cheek-teeth with vertical furrows that extend to the base of the crown and onto the root.

Description. UA 8653, the holotype specimen, is a molariform, hypsodont cheek-tooth (Fig. 2a). Its preserved height is 11.2 mm, and what are interpreted to be its length and width are 3.4 and 3.2 mm, respectively. The crown, as determined from the distribution of enamel, comprises about 85% of the tooth's height. UA 8653 is strongly curved along its height and worn flat on its occlusal surface. In occlusal view, the worn surface consists of a broad, V-shaped dentine island surrounded by enamel (except along one edge, where breakage has occurred). The indentation of the V is formed by a vertical furrow that extends through the entire height of the tooth and is filled with cementum. Enamel is clearly absent from one side of the crown, where two distinct, vertical enamel–dentine edges are evident. UA 8653 possesses small, circular enamel prisms aligned in rows, which are separated by prominent and continuous bands of interprismatic material (Fig. 2d).

FMNH PM 59520 (Fig. 2b) is tentatively referred to *L. miolaka*

Nature © Macmillan Publishers Ltd 1997